

UC Berkeley

UC Berkeley Previously Published Works

Title

X-ray scattering measurements of dissociation-induced metallization of dynamically compressed deuterium

Permalink

<https://escholarship.org/uc/item/2m54g19w>

Journal

Nature Communications, 7

Authors

Davis, P
Döppner, T
Rygg, JR
[et al.](#)

Publication Date

2016-04-15

DOI

10.1038/ncomms11189

Peer reviewed

ARTICLE

Received 15 May 2015 | Accepted 1 Mar 2016 | Published 15 Apr 2016

DOI: 10.1038/ncomms11189

OPEN

X-ray scattering measurements of dissociation-induced metallization of dynamically compressed deuterium

P. Davis^{1,2}, T. Döppner², J.R. Rygg², C. Fortmann^{2,3}, L. Divol², A. Pak², L. Fletcher⁴, A. Becker⁵, B. Holst⁵, P. Sperling⁵, R. Redmer⁵, M.P. Desjarlais⁶, P. Celliers², G.W. Collins², O.L. Landen², R.W. Falcone¹ & S.H. Glenzer⁴

Hydrogen, the simplest element in the universe, has a surprisingly complex phase diagram. Because of applications to planetary science, inertial confinement fusion and fundamental physics, its high-pressure properties have been the subject of intense study over the past two decades. While sophisticated static experiments have probed hydrogen's structure at ever higher pressures, studies examining the higher-temperature regime using dynamic compression have mostly been limited to optical measurement techniques. Here we present spectrally resolved x-ray scattering measurements from plasmons in dynamically compressed deuterium. Combined with Compton scattering, and velocity interferometry to determine shock pressure and mass density, this allows us to extract ionization state as a function of compression. The onset of ionization occurs close in pressure to where density functional theory-molecular dynamics (DFT-MD) simulations show molecular dissociation, suggesting hydrogen transitions from a molecular and insulating fluid to a conducting state without passing through an intermediate atomic phase.

¹University of California, Berkeley, California 94720, USA. ²Lawrence Livermore National Laboratory, PO Box 808, Livermore, California 94551, USA.

³University of California, Los Angeles, California 90095, USA. ⁴SLAC National Accelerator Laboratory, Menlo Park, California 94025, USA. ⁵Institut für Physik, Universität Rostock, D-18051 Rostock, Germany. ⁶Sandia National Laboratories, Albuquerque, New Mexico 87185, USA. Correspondence and requests for materials should be addressed to P.D. (email: pfdavis@berkeley.edu) or to S.H.G. (email: glenzer@slac.stanford.edu).

The insulator-metal transition in hydrogen has been a central problem in physics since Wigner and Huntington's 1935 prediction of a transformation of insulating molecular hydrogen to a monatomic conducting state at high pressure¹. In recent decades, owing to fundamental questions about the structure of gas giants^{2–6}, hydrogen's high-pressure properties have been the subject of intense study. Diamond anvil cell experiments have explored the low-temperature, high-pressure structure of hydrogen. It has been shown to remain in an insulating, molecular state at pressures in excess of 300 GPa (ref. 7) and recent work has focused on its phases near room temperature^{8–13}. Sophisticated *ab initio* simulation techniques have advanced in tandem, resulting in a wide computational exploration of the hydrogen phase diagram, see McMahon and coauthors¹⁴.

High-pressures produced by dynamic compression techniques generally result in higher-temperature conditions. Experiments using reverberating shock waves to produce conductive liquid hydrogen at 140 GPa and temperatures near 3,000 K (refs 15,16), reached densities very close to those predicted by Wigner and Huntington¹⁷. Recent experiments using the Sandia Z machine reached 300 GPa and 1,800 K, finding evidence for a liquid–liquid insulator-metal transition from optical reflectivity measurements¹⁸. In single-shock experiments, the temperatures reached are still higher, and the transition to metallic behaviour is driven by the combined pressure and temperature reached in the shock front. These experiments produce thermodynamic states lying on the primary shock Hugoniot. Optical reflectivity measurements have been used to observe a transition to metallic behaviour in laser-driven samples near 50 GPa and 8,000 K (ref. 19). X-ray scattering makes it possible to directly observe electron properties in such an experimental configuration, but until now it has not progressed beyond proof-of-principle in shock-compressed cryogenic samples²⁰. In this work, we use a single-shock laser compression scheme, employing x-ray scattering to directly measure the ionization of laser-shocked deuterium as a function of compression.

Dynamic experiments along the principal Hugoniot result in target conditions far from the region where a first-order

liquid–liquid phase transition from molecular to conducting fluids has been predicted^{21,22}. We illustrate this in the hydrogen phase diagram shown in Fig. 1, which shows that most parts of the interiors of brown dwarfs (Gliese-229b, shown in brown) and giant planets (Jupiter, shown in black) are also at off-Hugoniot states. However, the $P - T$ range of our experiments covers one of the most interesting parts of the Jovian interior. The flattening of the isentrope at ~ 25 GPa is due to the dissociation of the hydrogen molecules. As shown by French *et al.*²³, this is accompanied by a drastic increase in the dc electrical conductivity which represents a continuous nonmetal-to-metal transition. This result is validated with the x-ray scattering measurements presented in this study, where we find that the average ionization becomes significant just at this point on the Hugoniot curve, and coincident with dissociation. This is of great importance for planetary physics when validating equation of state (EOS) data that are used for interior^{2,23} and dynamo models²⁴.

Inelastic x-ray scattering has a long history as a powerful probe of material properties in static samples. Recently, x-ray scattering has been employed in high-energy density physics experiments²⁵ using laser-produced x-ray sources to measure density and temperature in targets dynamically shocked to warm, dense conditions^{26–29}. Experiments at the Omega laser have demonstrated the viability of backscattering techniques for density measurements in cryogenic deuterium²⁰. Here we combine forward and backward x-ray scattering observations with a simultaneous measurement of shock velocity using the velocity interferometry system for any reflector (VISAR) technique to infer pressure and mass density from the velocity of the shock and EOS tables. With a delocalized electron density measured using x-ray scattering, we can then directly determine the ionization state of shocked deuterium as a function of compression. We compare the onset of ionization with the molecular dissociation fraction calculated from density functional theory-molecular dynamics (DFT-MD) simulations and find that both quantities increase sharply between compressions of $2.5 \leq \rho/\rho_0 \leq 3.3$.

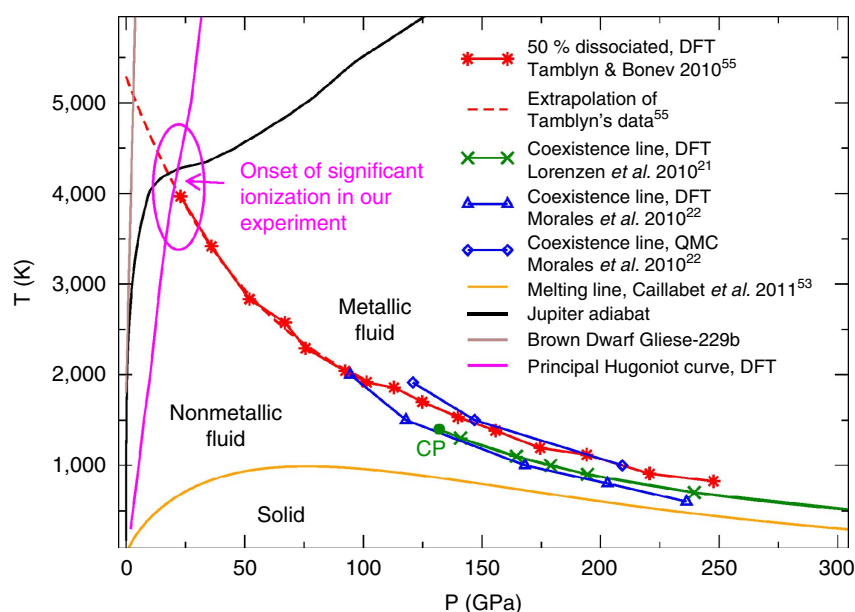


Figure 1 | Phase diagram of hydrogen. Displayed are the melting line⁵³ (orange), the isentropes of Jupiter^{2,23} (black) and the Brown Dwarf Gliese-229b (ref. 54) (brown), the principal Hugoniot curve (magenta) and results for the first-order liquid–liquid (plasma phase) transition (green²¹ and blue²²) together with predictions at which P - T points the system is dissociated by 50% (ref. 55) (red).

Results

Experiment design and layout. X-ray scattering is sensitive to both the electron and ion structure in the target. The scattering cross section depends on the total dynamic structure factor of the material that, in the case of dense plasma conditions, is often expressed using a chemical picture approach due to Chihara^{30,31} as $S_{ee}(k, \omega) = |f(k) + q(k)|^2 S_{ii}(k, \omega) + Z_f S_{ee}^0(k, \omega) + Z_b \int d\omega' \tilde{S}_{ce}(k, \omega - \omega') S_S(k, \omega')$. Here k is the wave-vector probed, $f(k)$ is the ionic form factor, $q(k)$ represents the electron screening cloud around the ion and Z_f (Z_b) is the number of free (bound) electrons per atom. S_{ii} and S_{ee}^0 represent the dynamic structure contributions of ions and free electrons; transitions of bound electrons into the continuum, S_{ce} , are modulated by the motion of the ions, represented by S_S .

In the non-relativistic limit, the probe energy and experimental geometry define the k -vectors probed according to $k = |\mathbf{k}| = 4\pi \frac{E_0}{hc} \sin(\theta/2)$. Our experiments probe density fluctuations at scale lengths of $k = 7.78 \times 10^9 \text{ m}^{-1}$ in the forward direction and $1.88 \times 10^{10} \text{ m}^{-1}$ in the backward direction. The

scattering process can be defined with the parameter $\alpha = 1/k\lambda_S$, where λ_S represents the screening length in the plasma. For the strongly degenerate systems studied in this work, the screening length can be approximated with the Thomas–Fermi length, and $\alpha = \frac{1}{k\lambda_S} = \frac{1}{k\lambda_{TF}} = \frac{1}{k} \sqrt{\frac{4m_e e^2}{h^2} \left(\frac{3n_e}{\pi}\right)^{1/3}}$ where n_e is the free-electron density. Thus, for our conditions, the forward scattering vector extends beyond the screening length and provides collective scattering even at small ionization fractions³², while the backward scattering vector is sufficiently long to probe at a scale length smaller than the screening length of the plasma, observing the electron momentum distribution in the Compton limit³³.

A series of cryogenic experiments was performed at the Janus Laser Facility at the Lawrence Livermore National Laboratory, a schematic of which is shown in Fig. 2. A drive laser was focused onto a cryogenic target, launching a shock wave into liquid deuterium at an initial density $\rho_0 = 0.17 \pm 0.004 \text{ g cm}^{-3}$. A second laser, incident on a Si_3N_4 foil fixed to the target at an intensity of $1 \times 10^{14} \text{ W cm}^{-2}$ and wavelength of 527 nm, created an intense x-ray source by pumping the 2keV Ly- α line in Si

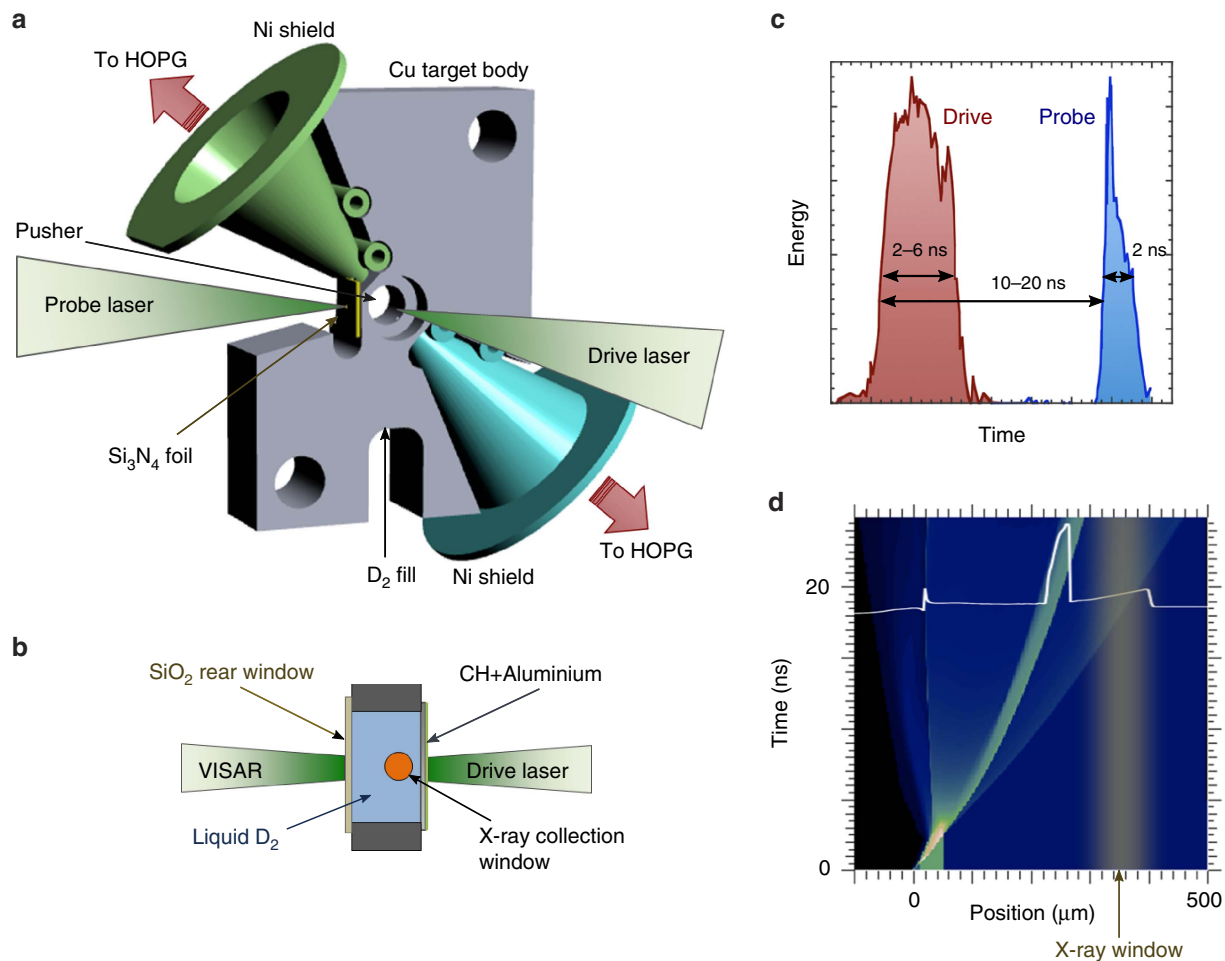


Figure 2 | Experimental set-up and timing. (a) The copper target is held at 19 K, liquefying the deuterium that is filled into the central cavity. A drive laser is incident on a 2-mm-diameter Al pusher, launching a shock wave along the axis. A probe laser irradiates a Si_3N_4 foil, pumping the 2,005 eV Si Ly- α transition. X-rays scattered in the forward and backward directions are spectrally dispersed with highly oriented pyrolytic graphite (HOPG) crystals whose direct view of the laser-plasma is prevented by Ni shields. (b) Cross section of the target reservoir across the thickness of the target. The target is sealed with aluminium on the front surface and a transparent quartz rear window to allow the VISAR beam to probe shock evolution. (c) Schematic of laser beam timing showing the shock drive beam (red) of 2–6 ns preceding a 2-ns probe pulse. The probe is delayed by 10–20 ns, depending on drive intensity, to allow the shock front to advance into the x-ray spectrometer view. Shorter delay times yielded higher shock pressures. (d) HYDRA simulations of mass density evolving as a function of space and time, with a lineout at the x-ray probe time of 20 ns. The compressed D_2 peak ($\rho_{\text{Shock}} = 0.54 \text{ g cm}^{-3}$) has traversed into the spectrometer field of view at $t = 20 \text{ ns}$ when we make the x-ray measurement. The high-density peak lagging the D_2 shock front is due to the aluminium pusher, but is shielded by the x-ray window.

(ref. 34; Supplementary Fig. 1 and Supplementary Methods). These photons were collimated through a 400- μm -diameter aperture in the target, timed to probe the shock as it reached the x-ray collection ports. The x-rays were scattered from the shock front and collected through 400 μm ports at 45° and 135° from the incident photons. The probe pulse was delayed 10–20 ns after the rise of the drive beam, allowing the shock to traverse a distance of 350 μm to reach the volume accessed by the x-ray diagnostic port. The fields of view of the spectrometers were shielded with Ni-coated cones (40° opening angle) from ambient x-ray emission and stray light from both laser beams. The radiation was collected and spectrally dispersed with highly ordered pyrolytic graphite crystal spectrometers³⁵ curved at a 107-mm radius.

The drive laser beam used a phase plate to produce a round 600- μm -diameter spot on target. The forward scattering measurements were made on deuterium shock-driven by a frequency-doubled 2-ns-long laser pulse producing a wavelength of 527 nm at the target. The backscattering measurements were made operating the same laser at the 1,054 nm fundamental. These shots used 4 ns drive pulses at moderate compression and 6 ns at higher compression, all at nominal intensities of $4 \times 10^{13} \text{ W cm}^{-2}$.

The drive laser was incident on a CH-coated aluminium layer ranging from 12 to 40 μm in thickness, depending on intended shock pressure. The CH layer was ablated in the laser-target interaction, driving a shock wave into the Al pusher that released into the D₂ layer. The aluminium shielded the bulk D₂ from hot electrons and x-rays produced in the laser-solid interaction that could preheat the target before the shock arrived.

Shock velocity and inferred compression. Since deuterium becomes optically reflective under shock compression, the shock velocity can be directly measured using the VISAR technique^{36,37}. For this purpose, we propagated a 532-nm VISAR probe beam anti-parallel to the drive beam along the axis of the shock through the rear window. The reflected signal from the D₂ shock front was collected and sent to two interferometers, coupled to optical streak cameras. These provided two 20-ns-long channels showing the evolution of shock velocity on each shot. Using two interferometers of differing sensitivities allowed the absolute velocity to be determined in spite of the discontinuity in phase caused by the shock.

To determine the mass density—and hence compression ρ/ρ_0 —of the target using measured shock velocity, one of two approaches is necessary. Impedance matching techniques can be used to determine particle velocity in addition to shock velocity, closing the Rankine–Hugoniot relations^{38–40} and directly constraining state variables in the target. Alternatively, existing theoretical models or measured EOS values can be used to calculate compression from the shock velocity measured with VISAR; that is the approach used in this study. While one of several modern EOS models could be effectively used, we have chosen the quotidian EOS (ref. 41) because of its computational efficiency and the fact that it represents a middle ground between popular EOS models in the pressure regime of interest. Because we rely on an EOS that is not perfectly known, this approach requires careful accounting for that uncertainty in our inferred compression. Hicks *et al.*⁴² gave a comparison of both calculated and measured EOS values and their associated experimental uncertainties. For our experimental conditions, variations in EOS models are relatively small; near 15 GPa, where we observe the onset of ionization, models vary by about 10% in compression at a given pressure (Supplementary Fig. 2 and Supplementary Methods). This uncertainty is included in the error bar of quoted values of mass density.

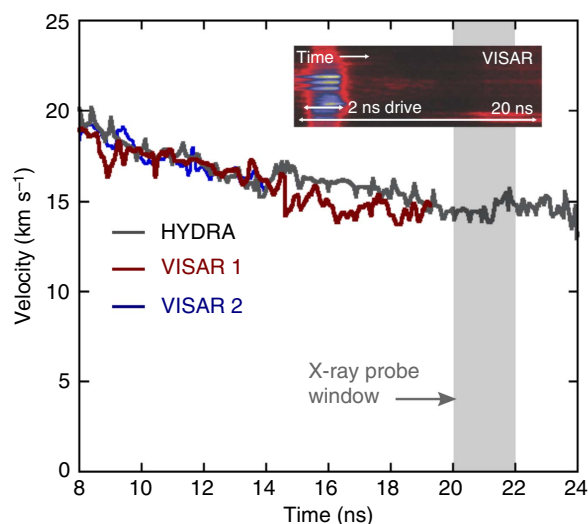


Figure 3 | VISAR shock velocity compares well with hydrodynamic simulations up to 20 ns when the x-ray probe begins.

We linearly extrapolate the mean velocity to obtain the average conditions during the x-ray probe. Uncertainty in shock velocity is estimated to be $\pm 1 \text{ km s}^{-1}$; uncertainty in timing is $\pm 0.5 \text{ ns}$. Inset: raw VISAR streak for one of two streak cameras. The bright pulse early in time comes from the drive beam. Breakout of the shock from the aluminium pusher into the deuterium occurs near the end of the drive beam, and the decaying shock velocity in D₂ is extracted from the fringes shifting in time.

Figure 3 shows a VISAR streak record along with the extracted shock velocities for high-power laser drive conditions. Also shown are simulation results from HYDRA, a radiation-hydrodynamics code widely used for modelling inertial confinement fusion and laser-plasma experiments⁴³. HYDRA accurately reproduces the measured late-time shock velocities when scattering is performed. Stray light from the drive beam is visible for 2 ns early in the streak. Shock breakout from the Al pusher into D₂ occurs near the end of the drive beam where a discontinuous fringe shift is visible. As the shock decays, a drop in signal amplitude is visible in the raw data, since reflectivity falls as shock pressure and ionization decrease. The peak velocity immediately following shock breakout from the pusher is 22 km s^{-1} with pressures near 50 GPa, which decays to $14 \pm 1 \text{ km s}^{-1}$ and $15 + 3.5 / - 4.5 \text{ GPa}$ at 21 ns, the centre of the 2-ns-long x-ray probe.

X-ray scattering spectra. Figure 4 shows collective scattering data measured with the forward spectrometer for two shock conditions. The upper spectrum is taken from the same shot as Fig. 3, with a compression of $\rho/\rho_0 = 3.2 + 0.2 / - 0.3$ at the time of x-ray probing, while the lower spectrum used a lower laser intensity drive to reach $\rho/\rho_0 = 2.8 + 0.3 / - 0.4$. At this lower drive condition, no inelastic feature is visible above the noise and spectral resolution of the detector, placing an upper bound on ionization state of $Z \leq 0.04$.

At the higher drive condition, a downshifted plasmon feature is visible centred at 1,998 eV below the probe energy of $E_0 = 2,005 \text{ eV}$. The plasmon resonance in this low-temperature regime experiences very little damping and is therefore quite narrow. The presented fit curves include broadening due to collisional effects calculated in the local-field-corrected Born-Mermin approximation, which goes beyond the random phase approximation to the dynamical structure factor by including electron–electron interactions and electron–ion collisions in the Born approximation^{27,44}. The spectrum is convolved

with the instrument function introduced by the highly ordered pyrolytic graphite crystal and detector. The broad low-energy tail may be explained by bound-free transitions, whose fit includes density- and temperature-dependent continuum lowering. A best fit to the data indicates a delocalized electron density of $n_e = 2.5 \pm 0.4 \times 10^{22} \text{ cm}^{-3}$ due to the free-electron density-sensitive plasmon shift at 7 eV. Combined with the mass density inferred from the VISAR trace, this corresponds to an average ionization state of $Z = 0.15 \pm 0.04$. The measured electron density corresponds to a Fermi temperature of $T_F = 3.1 \text{ eV}$. For typical temperatures of a fraction of an electron volt, the electrons are therefore strongly degenerate, with $\theta = kT/\varepsilon_F \sim 0.1$, and a scattering parameter of $\alpha = 1.5$.

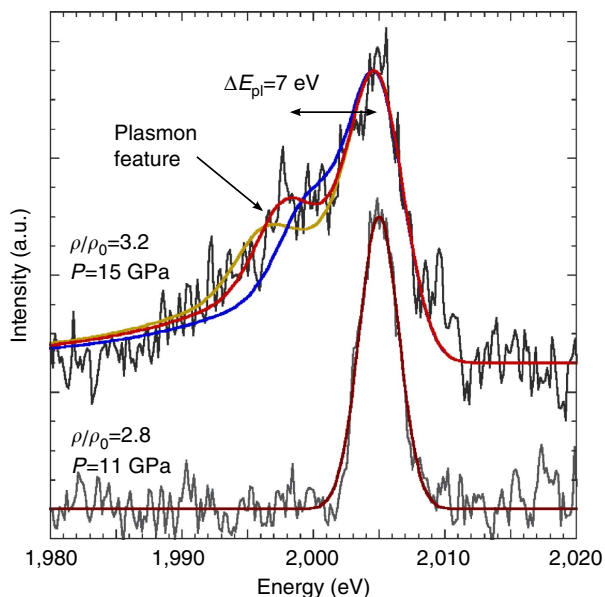


Figure 4 | Measured forward scattering spectra with theoretical fits. Pressure and compression are inferred from VISAR measurements. X-ray forward scattering spectrum from $3.2 \times$ shock-compressed D_2 showing elastic scatter at 2005 eV and downshifted plasmon with theoretical fits corresponding to $T_e = 0.15 \text{ eV}$ and $n_e = 1.3, 2.5$ (red) and 4.0 (yellow) $\times 10^{22} \text{ cm}^{-3}$. Below, a spectrum from $2.8 \times$ compressed D_2 showing no evidence of free electrons as a visible inelastic scattering feature.

Figure 5 shows the 135° backscattered spectrum from another shot using a 4-ns laser drive, and a probe beam delay of 15 ns. HYDRA calculations using an intensity profile matched to the velocity measurements shown above predict pressures of 16 GPa and compressions of $3.2 + 0.2 / - 0.4$, producing target conditions very close to those achieved in the plasmon scattering case. The ratio of elastic to inelastic scattering is strongly dependent on the ionization of the target; with increasing average ionization, the inelastic scattering contribution from free electrons grows relative to the remaining elastic signal. Fits are shown in Fig. 5a for ionizations $Z = 0.1-0.5$ and a best fit is achieved for $n_e = 2.4 \times 10^{22} \text{ cm}^{-3}$. This corresponds $Z = 0.15 \pm 0.08$, in good agreement with the plasmon data. At these conditions, the scattering parameter is $\alpha = 0.63$.

For non-collective scattering, the theoretical models used to describe the bound-free contribution can have a significant effect on the inelastic spectrum. In the present case where weakly bound electrons in the compressed deuterium occupy states near the continuum, continuum depression plays a particularly important role. To minimize any ambiguity introduced by this model dependence, we have compared our results, which use a Stewart-Pyatt (SP) model⁴⁵ for ionization potential depression, with a set of calculations using the Eckert-Kröll (EK) model⁴⁶. The resulting curves are shown in Fig. 5b, with the SP model in red and the EK model in blue. The contribution to the spectrum from bound-free scattering are shown separately as dashed curves, illustrating that the primary difference comes through the shift of the EK feature towards E_0 . We attribute this to a much higher value of continuum depression calculated by the EK model, $\Delta E_{EK} = 10.2 \text{ eV}$ compared with $\Delta E_{SP} = 2.1 \text{ eV}$ for SP. We note that in both cases a best fit is found for an ionization state of $Z = 0.15$ (Supplementary Figs 3 and 4 and Supplementary Methods). We conclude that, for very similar experimental drive conditions, plasmon and Compton scattering provide nearly identical ionization states; this is significant because the sensitivity of plasmon spectra and Compton scattering spectra to bound-free models and structure factors is very different. This finding indicates that contributions from bound-free scattering and interband transitions are accounted for by our data analysis and that interband transitions play a minor role in the interpretation of the data.

Discussion

Figure 6 summarizes measurements of ionization across several shock-drive and probe delay conditions producing compressions

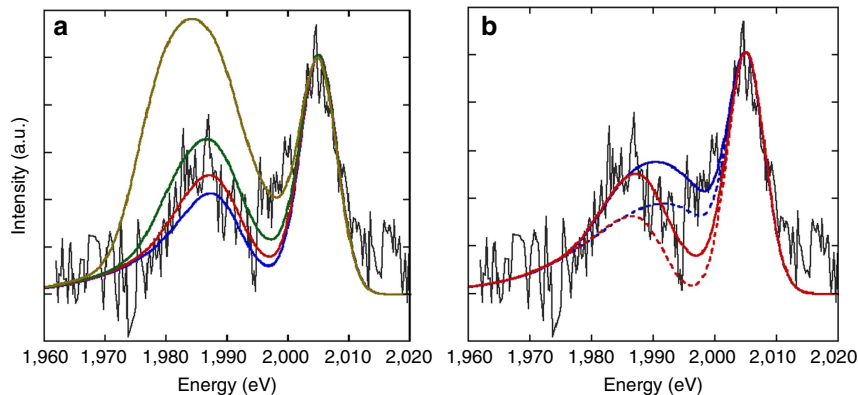


Figure 5 | Measured backscattering spectrum with theoretical fits. Fits are shown for target conditions of $T_e = 0.15 \text{ eV}$ and $\rho/\rho_0 = 3.2$. (a) Four ionization states corresponding to $Z = 0.1$ (blue), 0.15 (red), 0.25 (green) and 0.5 (yellow) are shown, with a best fit found for $n_e = 2.4 \times 10^{22} \text{ cm}^{-3}$ and $Z = 0.15 \pm 0.08$. (b) Theoretical fits for $Z = 0.15$ using the SP (red) and EK (blue) models for ionization potential depression. Solid lines correspond to the total spectrum and dashed to the elastic and bound-free scattering contributions without free-free scattering. Both models result in best fit values for ionization of $Z = 0.15$.

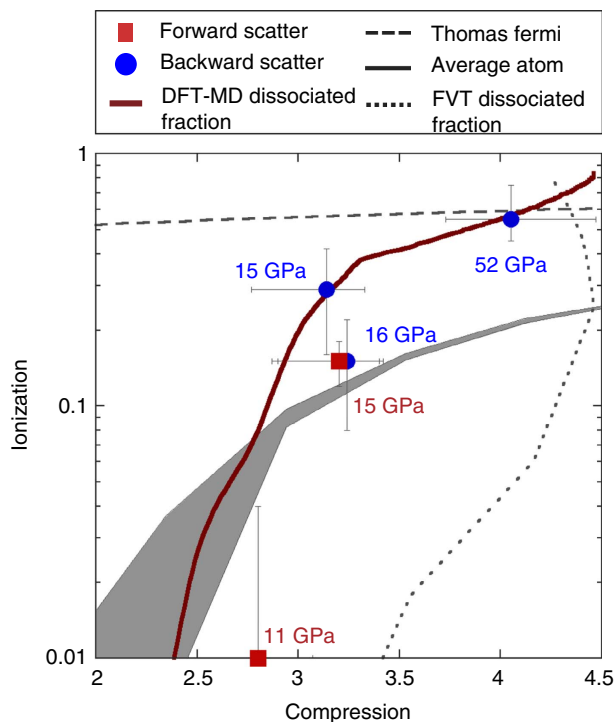


Figure 6 | Average ionization of D_2 plotted as a function of compression along the single-shock Hugoniot. Values of ionization inferred from plasmon measurements are shown as red squares, measurements using Compton scattering are shown as blue circles, and pressures from quotidian EOS (QEOS) are indicated for each data point. Ionization degree calculated with Thomas-Fermi theory is shown as a dashed line, while average-atom calculations are shown between a lower bound of $T_e = 0.1$ eV and an upper bound of $T_e = 0.5$ eV as a shaded region. The dark red line shows the molecular dissociation fraction calculated from density functional molecular dynamics simulations along the principal Hugoniot and the dotted line shows a similar dissociation calculation with the chemical picture code FVT. Measurements indicate a sharp increase in ionization near $3 \times$ compression, consistent with the DFT-MD calculated dissociated fraction.

between $\rho/\rho_0 = 2.8$ and $\rho/\rho_0 = 4.05$. Measured ionization states for both forward and backscattered configurations are shown as a function of compression, along with predicted ionizations from several models. The compression values for the backscattering data points and the lowest compression case, where velocity measurements are not possible below the onset of optical reflectivity, were determined using hydrodynamic calculations benchmarked to VISAR measurements. The error bars in compression for these points include a 20% uncertainty in drive intensity and uncertainty between EOS models at the relevant pressures. The data indicate a sharp onset of ionization between 3 and 3.5 times compression.

This onset is reproduced by average-atom simulations of a D ion system embedded in a plasma background⁴⁷, but with lower absolute ionization values. The Thomas-Fermi model exhibits very little of the density dependence in the data at low compression. Similar results have been reported in x-ray scattering experiments on shock-compressed CH (ref. 48). We also show the deuterium dissociation curve calculated with the code FVT, a chemical picture model based on fluid variational theory⁴⁹ that predicts the onset of molecular dissociation at higher compressions than measured here.

Theoretical models for dense matter can be divided into chemical and physical-picture models. In the chemical picture, ions, atoms and molecules are treated as elementary members of the ensemble, while in the physical picture, nuclei and electrons are treated as elementary particles and bound states are long-lived correlations between them. While ab initio physical picture theories represent the state-of-the-art in simulating hydrogen under extreme conditions, an explicit definition of ionization within a physical-picture model is difficult in pressure and temperature regimes where electron delocalization and finite temperatures blur the characteristics of free and bound electrons. To provide a comparison to our measurements we have calculated the dissociation of deuterium molecules along the Hugoniot using DFT-MD (ref. 50). DFT-MD couples a finite-temperature treatment of electrons using density functional theory with a molecular dynamics treatment of ion motion. The dissociated fraction, shown in red in Fig. 6, is estimated by tracking neighbouring ions in the system as the simulation evolves in time (Supplementary Figs 5 and 6 and Supplementary

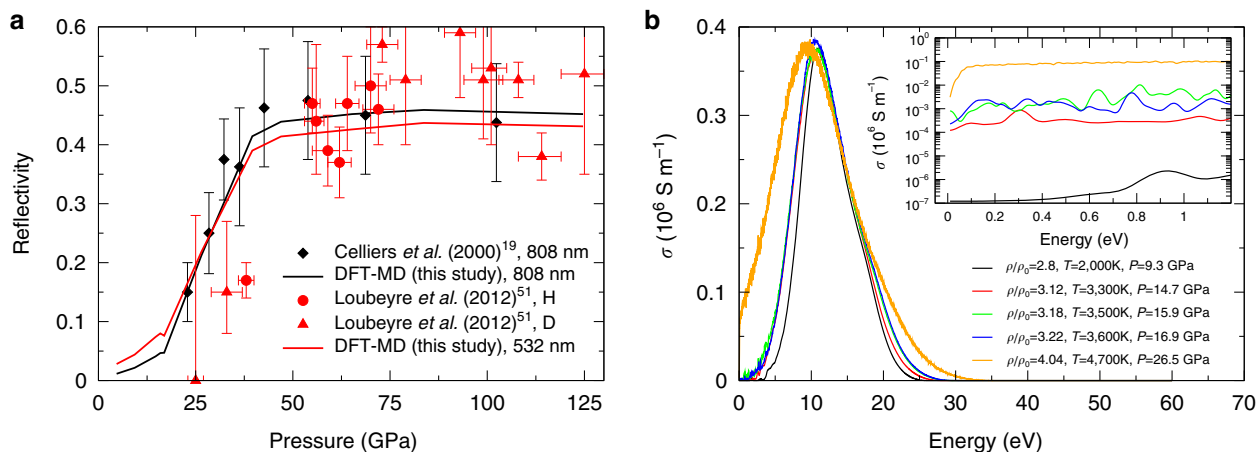


Figure 7 | Reflectivity and conductivity calculated from DFT-MD simulations. (a) Reflectivities along the principal Hugoniot curve for 808 nm from the experiments of Celliers *et al.* (black diamonds) and DFT-MD calculations in this work (solid black line). Reflectivities for 532 nm from the experiments of Loubeyre *et al.* in hydrogen (red dots) and deuterium (red triangles) and DFT-MD calculations in this work (solid red line). (b) Dynamic electrical conductivity at the five experimental points for which the thermodynamic states along the principal Hugoniot curve are given in the legend. The dc limit ($\omega \rightarrow 0$) is displayed in the inset.

Methods). The fraction of dissociated molecules in the calculations matches the fraction of measured ions closely, suggesting that the processes of dissociation and ionization occur nearly simultaneously along the Hugoniot, see also refs 21–23.

To facilitate further comparison between our simulations and experimental results, optical reflectivity and dynamic conductivity were calculated from the DFT-MD results. Figure 7a shows reflectivity calculated along the principal Hugoniot (Supplementary Fig. 7 and Supplementary Note 1). Comparisons are made at 808 nm with the results of Celliers *et al.*¹⁹ and at 532 nm with the recent measurements by Loubeyre *et al.*⁵¹. Good agreement is found between experiment and theory. Between 20 and 50 GPa, DFT-MD is seen to produce somewhat higher reflectivities than the Loubeyre results, attributable to the fact that DFT-MD underestimates the bandgap systematically using exchange-correlation functionals like that of Perdew, Burke, and Ernzerhof (ref. 52), leading to early bandgap closure and an earlier onset of dissociation and, thereby, conduction. In Fig. 7b, the dynamic conductivity along the Hugoniot is plotted at a pressure range corresponding to our experimental conditions. The DC limit is plotted in the inset, showing that conductivity starts at very small values near 0.1 S m^{-1} at $2.8 \times$ compression (black curve), rising orders of magnitude to a metallic conductivity of 10^5 S m^{-1} near fourfold compression (yellow curve). This confirms the continuous transition from an insulating molecular fluid to a metallic degenerate electron liquid observed in the experiments.

More broadly, this work demonstrates the viability of combining x-ray spectroscopic and optical velocity measurements to make detailed inferences into the electronic states of a variety of materials compressed to pressures relevant to planetary science. As fourth-generation light sources come online, we expect these results to lead to an unprecedented exploration of the high-pressure structure of hydrogen and other light elements and allow experimental determination of such properties as interior temperature profiles and core erosion in giant planets.

References

- Wigner, E. & Huntington, H. B. On the possibility of a metallic modification of hydrogen. *J. Chem. Phys.* **3**, 764–770 (1935).
- Guillot, T. Interiors of giant planets inside and outside the solar system. *Science* **286**, 72–77 (1999).
- Nettelman, N., Holst, B., Kietzmann, A., French, M. & Redmer, R. Ab initio equation of state data for hydrogen, helium, and water and the internal structure of Jupiter. *Astrophys. J.* **683**, 1217–1228 (2008).
- Wilson, H. F. & Militzer, B. Rocky Core solubility in Jupiter and giant exoplanets. *Phys. Rev. Lett.* **108**, 111101 (2012).
- Nellis, W. J., Weir, S. T. & Mitchell, A. C. Metallization and electrical conductivity of hydrogen in Jupiter. *Science* **273**, 936–938 (1996).
- Vorberger, J., Tamblyn, I., Militzer, B. & Bonev, S. A. Hydrogen-helium mixtures in the interiors of giant planets. *Phys. Rev. B* **75**, 024206 (2007).
- Loubeyre, P., Ocelli, F. & LeToullec, R. Optical studies of solid hydrogen to 320 GPa and evidence for black hydrogen. *Nature* **416**, 613–617 (2002).
- Eremets, M. I. & Troyan, I. A. Conductive dense hydrogen. *Nat. Mater.* **10**, 927–931 (2011).
- Eremets, M. I., Troyan, I. A., Lerch, P. & Drozdov, A. Infrared study of hydrogen up to 310 GPa at room temperature. *High Press. Res.* **33**, 377–380 (2013).
- Zha, C. S., Liu, Z. & Hemley, R. J. Synchrotron infrared measurements of dense hydrogen to 360 GPa. *Phys. Rev. Lett.* **108**, 146402 (2012).
- Zha, C., Cohen, R. E., Mao, H. & Hemley, R. J. Raman measurements of phase transitions in dense solid hydrogen and deuterium to 325 GPa. *Proc. Natl Acad. Sci. USA* **111**, 4792–4797 (2014).
- Cohen, R. E., Naumov, I. I. & Hemley, R. J. Electronic excitations and metallization of dense solid hydrogen. *Proc. Natl Acad. Sci. USA* **110**, 13757–13762 (2013).
- Howe, R. T., Guillaume, C. L., Scheler, T., Goncharov, A. F. & Gregoryanz, E. Mixed molecular and atomic phase of dense hydrogen. *Phys. Rev. Lett.* **108**, 125501 (2012).
- McMahon, J. M., Morales, M. A., Pierleoni, C. & Ceperley, D. M. The properties of hydrogen and helium under extreme conditions. *Rev. Mod. Phys.* **84**, 1607–1653 (2012).
- Weir, S. T., Mitchell, A. C. & Nellis, W. J. Metallization of fluid molecular hydrogen at 140 GPa (1.4 Mbar). *Phys. Rev. Lett.* **76**, 1860 (1996).
- Nellis, W. J., Weir, S. T. & Mitchell, A. C. Minimum metallic conductivity of fluid hydrogen at 140 GPa (1.40 Mbar). *Phys. Rev. B* **59**, 3434–3449 (1999).
- Nellis, W. J. Wigner and Huntington: the long quest for metallic hydrogen. *High Press. Res.* **33**, 369–376 (2013).
- Knudson, M. D. *et al.* Direct observation of an abrupt insulator-to-metal transition in dense liquid deuterium. *Science* **348**, 1455–1460 (2015).
- Celliers, P. M. *et al.* Shock-induced transformation of liquid deuterium into a metallic fluid. *Phys. Rev. Lett.* **84**, 5564 (2000).
- Regan, S. *et al.* Inelastic X-Ray scattering from shocked liquid deuterium. *Phys. Rev. Lett.* **109**, 265003 (2012).
- Lorenzen, W., Holst, B. & Redmer, R. First-order liquid-liquid phase transition in dense hydrogen. *Phys. Rev. B* **82**, 195107 (2010).
- Morales, M. A., Pierleoni, C., Schwegler, E. & Ceperley, D. M. Evidence for a first-order liquid-liquid transition in high-pressure hydrogen from ab initio simulations. *Proc. Natl Acad. Sci. USA* **107**, 12799–12803 (2010).
- French, M. *et al.* Ab initio simulations for the material properties along Jupiter's adiabat. *Astrophys. J. Suppl. Ser.* **202**, 5 (2012).
- Gastine, T., Wicht, J., Duarte, L. D. V., Heimpel, M. & Becker, A. Explaining Jupiter's magnetic field and equatorial jet dynamics. *Geophys. Res. Lett.* **41**, 5410 (2014).
- Glenzer, S. H. & Redmer, R. X-ray Thomson scattering in high energy density plasmas. *Rev. Mod. Phys.* **81**, 1625–1663 (2009).
- Kritcher, A. L. *et al.* Ultrafast X-ray Thomson scattering. *Science* **322**, 69–71 (2008).
- Neumayer, P. *et al.* Plasmons in strongly coupled shock-compressed matter. *Phys. Rev. Lett.* **105**, 075003 (2010).
- Fortmann, C. *et al.* Measurement of the heat capacity ratio in shock compressed Be. *Phys. Rev. Lett.* **108**, 175006 (2012).
- Garcia-Saiz, E. *et al.* Probing warm dense lithium by inelastic X-ray scattering. *Nat. Phys.* **4**, 940–944 (2008).
- Chihara, J. Interaction of photons with plasmas and liquid metals—photoabsorption and scattering. *J. Phys. Condens. Matter* **12**, 231 (2000).
- Gregori, G., Glenzer, S. H., Rozmus, W., Lee, R. W. & Landen, O. L. Theoretical model of x-ray scattering as a dense matter probe. *Phys. Rev. E* **67**, 026412 (2003).
- Glenzer, S. H. *et al.* Observations of plasmons in warm dense matter. *Phys. Rev. Lett.* **98**, 065002 (2007).
- Glenzer, S. H. *et al.* Demonstration of spectrally resolved X-Ray scattering in dense plasmas. *Phys. Rev. Lett.* **90**, 175002 (2003).
- Davis, P., Döppner, T., Glenzer, S. H., Falcone, R. W. & Unites, W. An apparatus for the characterization of warm, dense deuterium with inelastic x-ray scattering. *JINST* **7**, 02004 (2012).
- Pak, A. *et al.* X-ray line measurements with high efficiency Bragg crystals. *Rev. Sci. Instrum.* **75**, 3747–3749 (2004).
- Celliers, P. M. *et al.* Line-imaging velocimeter for shock diagnostics at the OMEGA laser facility. *Rev. Sci. Instrum.* **75**, 4916–4929 (2004).
- Falk, K. *et al.* Comparison between x-ray scattering and velocity-interferometry measurements from shocked liquid deuterium. *Phys. Rev. E* **87**, 043112 (2013).
- Collins, G. W. *et al.* Measurements of the equation of state of deuterium at the fluid insulator-metal transition. *Science* **281**, 1178–1181 (1998).
- Knudson, M. D. *et al.* Equation of state measurements in liquid deuterium to 70 GPa. *Phys. Rev. Lett.* **87**, 225501 (2001).
- Knudson, M. D. *et al.* Principal Hugoniot, reverberating wave, and mechanical shock measurements of liquid deuterium to 400 GPa using plate impact techniques. *Phys. Rev. B* **69**, 144209 (2004).
- More, R. M., Warren, K. H., Young, D. A. & Zimmerman, G. B. A new quotidian equation of state (QEOS) for hot dense matter. *Phys. Fluids* **31**, 3059–3078 (1988).
- Hicks, D. G. *et al.* Laser-driven single shock compression of fluid deuterium from 45 to 220 GPa. *Phys. Rev. B* **79**, 014112 (2009).
- Marinak, M. M. *et al.* Three-dimensional simulations of Nova high growth factor capsule implosion experiments. *Phys. Plasmas* **3**, 2070 (1996).
- Redmer, R., Reinholz, H., Röpke, G., Thiele, R. & Höll, A. Theory of X-Ray Thomson scattering in dense plasmas. *IEEE Trans. Plasma Sci.* **33**, 77–84 (2005).
- Stewart, J. C. & Pyatt, Jr K. D. Lowering of ionization potentials in plasmas. *Astrophys. J.* **144**, 1203 (1966).
- Ecker, G. & Kröll, W. Lowering of the ionization energy for a plasma in thermodynamic equilibrium. *Phys. Fluids* **6**, 62 (1963).
- Johnson, W. R., Guet, C. & Bertsch, G. F. Optical properties of plasmas based on an average-atom model. *J. Quant. Spectrosc. Radiat. Transf.* **99**, 327 (2006).

48. Fletcher, L. B. *et al.* Observations of continuum depression in warm dense matter with X-Ray Thomson scattering. *Phys. Rev. Lett.* **112**, 145004 (2014).
49. Holst, B., Nettelmann, N. & Redmer, R. Equation of state for dense hydrogen and plasma phase transition. *Contrib. Plasma Phys.* **47**, 368–374 (2007).
50. Holst, B., Redmer, R. & Desjarlais, M. P. Thermophysical properties of warm, dense hydrogen using quantum molecular dynamics simulations. *Phys. Rev. B* **77**, 184201 (2008).
51. Loubeyre, P. *et al.* Extended data set for the equation of state of warm dense hydrogen isotopes. *Phys. Rev. B* **86**, 144115 (2012).
52. Perdew, J. P., Burke, K. & Ernzerhof, M. Generalized gradient approximation made simple. *Phys. Rev. Lett.* **77**, 3865 (1996).
53. Caillabet, L., Mazevet, S. & Loubeyre, P. Multiphase equation of state of hydrogen from ab initio calculations in the range 0.2 to 5 g/cc up to 10 eV. *Phys. Rev. B* **83**, 094101 (2011).
54. Becker, A. *et al.* Ab initio equations of states for hydrogen (H-REOS.3) and helium (He-REOS.3) and their implications for the interiors of brown dwarfs. *Astrophys. J. Suppl. Ser.* **215**, 21 (2014).
55. Tamblyn, I. & Bonev, S. A. Structure and phase boundaries in compressed liquid hydrogen. *Phys. Rev. Lett.* **104**, 065702 (2010).

Acknowledgements

The authors thank the Jupiter Laser Facility staff for facility support and W. Unites for target development and experimental support. This work performed under the auspices of the (US) Department of Energy (DOE) by Lawrence Livermore National Laboratory (LLNL) under Contract No. DE-AC52-07NA27344 and supported by Laboratory Directed Research and Development (LDRD) Grant 11-ER-050. P.D. was supported by the NNSA SSGF programme. A.B., B.H., P.S. and R.R. acknowledge support from the Deutsche Forschungsgemeinschaft (DFG) within the SFB 652 and the BMBF via the FSP-301. A.B. performed calculations within the grant mvp00008 at the North-German

Supercomputing Alliance (HLRN). This work was supported by DOE Office of Science, Fusion Energy Science under FWP 100182.

Author contributions

P.D., T.D., J.R.R., A.P. and L.F. performed the experiments. P.D., J.R.R. and S.H.G. analysed the data. C.F., A.B., B.H., P.S. and R.R. performed simulations of ionization, dissociation, reflectivity and conductivity; L.D. performed hydrodynamic simulations. P.C., G.W.C., M.P.D., O.L.L., R.W.F., R.R. and S.H.G. provided additional support for experiment design, analysis and interpretation. P.D. and S.H.G. wrote the paper.

Additional information

Supplementary Information accompanies this paper at <http://www.nature.com/naturecommunications>

Competing financial interests: The authors declare no competing financial interests.

Reprints and permission information is available online at <http://npg.nature.com/reprintsandpermissions/>

How to cite this article: Davis, P. *et al.* X-ray scattering measurements of dissociation-induced metallization of dynamically compressed deuterium. *Nat. Commun.* **7**:11189 doi: 10.1038/ncomms11189 (2016).



This work is licensed under a Creative Commons Attribution-NonCommercial-NoDerivs 4.0 International License. The images or other third party material in this article are included in the article's Creative Commons license, unless indicated otherwise in the credit line; if the material is not included under the Creative Commons license, users will need to obtain permission from the license holder to reproduce the material. To view a copy of this license, visit <http://creativecommons.org/licenses/by-nc-nd/4.0/>